Title

Structure of a monolayer of molecular rotors on aqueous subphase from grazing-incidence X-ray diffraction

Journal
Proceedings of the National Academy of Sciences of the United States of America, 115(38)

ISSN
0027-8424

Authors
Kaleta, Jiří
Wen, Jin
Magnera, Thomas F
et al.

Publication Date
2018-09-18

DOI
10.1073/pnas.1712789115

Peer reviewed

SPECIAL FEATURE

Structure of a monolayer of molecular rotors on aqueous subphase from grazing-incidence X-ray diffraction

Jiří Kaleta[a,b], Jin Wen[a], Thomas F. Magnera[b], Paul I. Dron[b], Chenhui Zhu[c], and Josef Michl[a,b,1]

[a]Institute of Organic Chemistry and Biochemistry, Academy of Sciences of the Czech Republic, 16610 Prague 6, Czech Republic; [b]Department of Chemistry and Biochemistry, University of Colorado Boulder, Boulder, CO 80309; and [c]Advanced Light Source, Lawrence Berkeley National Laboratory, Berkeley, CA 94720

Edited by J. Fraser Stoddart, Northwestern University, Evanston, IL, and approved February 8, 2018 (received for review September 30, 2017)

In situ grazing-incidence X-ray scattering shows that a monolayer of artificial rod-shaped dipolar molecular rotors produced on the surface of an aqueous subphase in a Langmuir trough has a structure conducive to a 2D ferroelectric phase. The axes of the rotors stand an average of 0.83 nm apart in a triangular grid, perpendicular to the surface within experimental error. They carry 2,3-dichlorophenylene rotators near rod centers, between two decks of interlocked triptycenes installed axially on the rotor axle. The analysis is based first on simultaneous fitting of observed Bragg rods and second on fitting the reflectivity curve with only three adjustable parameters and the calculated rotor electron density, which also revealed the presence of about seven molecules of water near each rotator. Dependent on preparation conditions, a minor and variable amount of a different crystal phase may also be present in the monolayer.

grazing-incidence X-ray scattering | X-ray reflectivity | molecular rotors | aqueous-surface monolayer | synchrotron radiation

We have been examining 2D assemblies of dipolar molecular rotors in an effort to detect collective behavior (1). Ultimately, we hope to produce an artificial 2D ferroelectric phase of dipolar azimuthal molecular rotors located on a flat electrical insulator, both for fundamental investigations and for its possible applications in nanoscience.

To meet this goal, theory (2) suggests that the rotors should be assembled in a trigonal lattice. The surface assembly is expected to be ferroelectric between the Debye temperature T_D, below which rotational barriers prevent the rotors from turning, and the Curie temperature T_C, above which thermal disorder dominates. The former condition calls for small rotational barriers, no higher than 1–2 kcal/mol [in 3D assemblies, rotational barriers as low as 0.7 kcal/mol have been achieved (3)]. The latter condition requires large rotatable dipoles μ spaced a small distance a apart, since T_C is expected to be proportional to μ^2/a^3.

After dealing with surface inclusions, in which molecular rotors were contained on the surface of a host crystal, and detecting ferroelectric interactions but no ferroelectric phase in bulk inclusions (4), we are now also exploring monolayers produced on aqueous surfaces using a Langmuir–Blodgett (LB) trough (5) and molecular rotors designed to assemble into a trigonal lattice (6). The hope is that the rotor axes will be perpendicular to the surface and separated by a small lattice constant ($a < 1$ nm) and that large monocrystalline domains can be produced. Ultimately, a monolayer of a suitable structure is to be transferred from the aqueous surface to a solid substrate for further study, possibly only after cross-linking for increased sturdiness.

Many organic materials pack closely at the air–water interface. Their unit cells tend to be tilted and distorted (7–19), but some nearly perfectly straight structures have also been observed (20). We were inspired by close-packed LB films of fatty acids, which have trigonal lattices and preserve them upon transfer to solid substrates (20–23).

To encourage trigonal packing (24–34) and perpendicular orientation on an aqueous surface while keeping dipole rotation nearly unhindered we prepared (6) the rod-shaped molecular rotor **1** (Fig. 1). It carries a terminal carboxylic acid group and a dipolar rotator (2,3-dichloro-1,4-phenylene) between two Y-shaped axial triptycene units, designed to form two decks of interlocked triptycenes. We now report grazing-incidence X-ray diffraction (GIXD) (14, 35) evidence that a monolayer of **1** indeed forms and has the desired structure.

Results

GIXD for a Monolayer of 1 on an Aqueous Subphase. Langmuir isotherms indicate that upon compression **1** has an extrapolated mean molecular area (mmA) of 63 ± 3 Å^2, compatible with the hoped-for packing (Fig. S1).

Table 1 summarizes the information obtained by GIXD, analyzed as explained in *Analysis of GIXD Data*. Scattering intensity (Fig. S2) is mapped against the xy component of the reciprocal scattering vector $\boldsymbol{Q}$ and is related to the azimuthal scattering angle 2θ by $Q_{xy} = (4\pi/\lambda)\sin\theta$, where λ is the wavelength. Fig. 2 shows the integrated intensity cut. The broad underlying baseline structure that grows in intensity for $Q_{xy} = 1.2–2.5$ and then slowly falls is scattering from bulk water (36). Intensities listed in Table 1 are measured locally with the background scattering from water removed. The size of the crystalline domains can be estimated from the formula (11) for the coherence or correlation length, $\ell = 0.9 \times 2\pi/Q_{xy}$ (FWHM), and since in most cases FWHM is

Significance

The so-far-unknown 2D ferroelectric assemblies of dipolar molecular rotors would be of considerable interest for miniaturization of analog electronics. We have prepared a monolayer of such rod-shaped rotors on an aqueous surface and used grazing-incidence X-ray scattering to determine that its structure meets theoretical requirements for ferroelectricity perfectly. The dipoles, averaged between the three nearest neighbors, stand 0.83 nm apart in a horizontal triangular grid and their rotation axes are vertical. One deck of interlocked triptycenes is located above and one below the dipoles, and on the average seven molecules of water are present near each dipole. It remains to be seen whether the structure can be transferred to an insulator surface undisturbed and is indeed ferroelectric.

Author contributions: J.M. designed research; J.K., J.W., T.F.M., P.I.D., C.Z., and J.M. performed research; and J.K., J.W., T.F.M., and J.M. wrote the paper.

The authors declare no conflict of interest.

This article is a PNAS Direct Submission.

[1]To whom correspondence should be addressed. Email: josef.michl@colorado.edu.

This article contains supporting information online at www.pnas.org/lookup/suppl/doi:10.1073/pnas.1712789115/-/DCSupplemental.

Published online March 23, 2018.

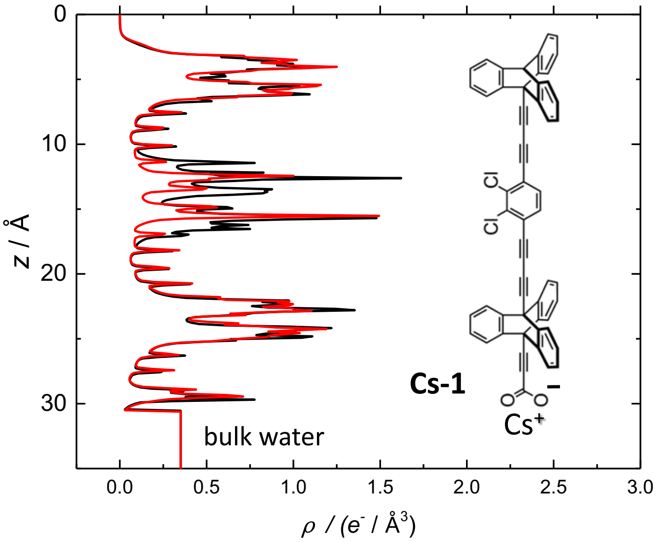

Fig. 1. (*Right*) Chemical structure of the dipolar molecular rotor **1**. (*Left*) Electron density profiles normal to the water surface for the rotor unhydrated (red) and hydrated by seven water molecules (black) with optimized positions between the triptycene layers.

resolution-limited a value of ~43 nm as a lower limit to the domain size is obtained.

The Two Lattices. The observations suggest the presence of two types of crystalline domains. Two groups of peaks are present, indexed in red and in blue in Fig. 2 and listed separately in Table 1. The relative intensity of peaks within each group is always similar, but the relative intensity of the two groups varies with details of monolayer preparation, such as surface pressure, compression rate, and choice of the spreading solvent and counter ions. The two groups can be separately indexed with two distinct unit cells defining two different incommensurate lattices.

The group of two strong broad peaks and three weaker peaks that dominates at high surface pressures defines the major lattice. The remaining nine weak peaks are assigned to the minor lattice. There probably are other peaks in the latter group that are difficult to discern from noise.

Major Lattice. The peaks in Fig. 2 indexed in red are assigned to a hexagonal lattice system (Table 1). The unit cell parameters were initially estimated by indexing the two strongest peaks and refined by recognizing that the peaks centered at Q_{xy} = 0.88 and 1.51 are too broad to be a single peak given the 0.013-$Å^{-1}$ resolution but may each be fitted with three Gaussians using a single constraint (FWHM = 0.013 $Å^{-1}$; Fig. 3 *E* and *F*). Indexing peaks near Q_{xy} = 0.88 as {0,1},{1,0}, {−1,1} and those near Q_{xy} = 1.50 as {1,1}, {−1,2}, {−2,1} leads to the assignment {0,2}, {2,0}, {−2,2} for the band near Q_{xy} = 1.72. Unit cell parameters were finally optimized by a least-squares fit to the resulting expanded and complete set of 14 observable Bragg peaks, yielding a triangular lattice with a rhombic primitive unit cell of dimensions 8.13 ± 0.01 Å × 8.40 ± 0.02 Å, an angle of 119.7 ± 0.2°, and an area per rotor A = 59.4 $Å^2$.

Using the form factor $F(\boldsymbol{Q})$, where $\rho(\boldsymbol{r}) = \rho_0[1 - \cos(3\theta)]$ is the electron density for $\boldsymbol{r} < \boldsymbol{r}_0$, and zero elsewhere, $\boldsymbol{r}_0$ is the rotor radius, and L is the rotor length (*Supporting Information*),

$$F(\boldsymbol{Q}) = F(Q_{hk}, Q_z) = \int_0^{r_0}\int_0^{2\pi} \rho_0\{1-\cos[3(\theta+\theta_{hk})]\} \times \exp(iQ_{hk}\, r\cos\theta) r\mathrm{d}r\mathrm{d}\theta \int_0^{L} \exp(iQ_z\, z)\,\mathrm{d}z, \quad [1]$$

a fit to Eq. **1** of the Bragg rod profiles for the two strongest peaks of the major lattice (Fig. 3) yielded the twist (α), tilt (*t*), and tilt

Table 1. Diffraction peaks observed for a monolayer of 1 on 10 mM aqueous CsCl

Lattice	*h*	*k*	Q_{hk} (observed)	Q_{hk} (observed/fit)	Q_{hk} (calculated)	I_{hk} (observed)	I_{hk} (calculated)
Major lattice	0	1		0.867 ± 0.003*	0.861	556 ± 8%†	744 ± 14%†
	1	−1	0.876‡	0.881	0.880	8,387	760
	1	0		0.890	0.890	771	723
	1	−2		1.499	1.500	1,400	1,156
	1	1	1.51§	1.510	1.514	2,200	2,412
	2	−1		1.530	1.546	1,767	1,542
	0	2	1.72		1.722	429	340
	2	−2	1.75		1.760	336	214
	2	0	1.77		1.779	122	220
	1	−3			2.277	0	14
	2	−3	2.24		2.299	55	2.5
	2	1			2.329	0	27
	3	−2	2.35		2.352	121	15
	3	−1	2.36		2.364	121	3.4
Minor lattice	1	0	0.47 ± 0.01*		0.467	190 ± 8%†	
	1	−1	0.68		0.703	162	
	0	1	0.77		0.759	298	
	2	−1	0.92		0.921		
	2	0	0.94		0.933	443	
	1	1	1.05		1.046	316	
	3	0	1.40		1.400	400	
	2	1	1.46		1.430	494	
	4	−1	1.63		1.692	340	

*SE.
†SE×100/*I*.
‡Found by fitting the broad peak at *Q* = 0.88 with three Gaussian peaks constrained to FWHM of 0.013 $Å^{-1}$.
§Found by fitting the broad peak at *Q* = 1.51 with three Gaussian peaks constrained to FWHM of 0.013 $Å^{-1}$ (Fig. 3 *E* and *F*).

Table 2. X-ray reflectivity: Parameters for model B

Subunit	L (calculated)/Å	L(fit)/Å*	n_e†	n_e (fit)	ρ e^-/Å^3	σ(fit)/Å
He			0		0	3.87 ± 0.014†
$C_{20}H_{13}$	5	5.09 ± 0.10‡	133	133	0.437	7.90 ± 0.085
C_4	5	3.00 ± 0.08	24	18	0.100	4.72 ± 0.047
$C_6H_2Cl_2$	4	5.35 ± 0.07	72	106	0.334	14.0 ± 0.21
C_4	4	2.72 ± 0.07	24	16	0.100	7.4 ± 0.061
$C_{20}H_{12}$	5	4.53 ± 0.11	132	114	0.39	9.90 ± 0.040
C_3O_2Cs	4.8	3.84 ± 0.05	89	86	0.494	8.85 ± 0.039
Subphase	∞				0.334	
Total	27.8	24.53	474	473		

*The software for the reflectivity calculations was provided by the ChemMAT/CARS facility at the Advanced Photon Source, Argonne National Laboratory.
†Number of electrons.
‡SE.

direction (ψ) of the rotor (Fig. S3). Their variation with Q_z contains information about the magnitude and direction of t, and the profile for each $\{h,k\}$ follows $F(Q_{hk})$ and is sensitive to α and ψ. We noted that the latter pair of angles is strongly determined by the relative intensity of the 0.88 group to the 1.51 group. For perfectly vertical rotors the Bragg rod profile would be given by the interfacial-surface electric-field correction factor defined (37) as $V(Q_z) = 2x/[x + (x^2 - 1)^{1/2}]$ for $x > 1$ and $V(Q_z) = 2x$ for $0 < x \leq 1$, where $x = Q_z/Q_c$ and $Q_c = 0.021764$ Å^{-1} for neat water (38) at λ = 1.23984 Å, increasing slightly and directly with the electron density of the subphase. Their relative intensity at different Q_{hk} is still modulated through $F(\boldsymbol{Q})$. The Bragg rod profiles for the overlapping peaks at $Q_z = 0.88$ {1,0},{0,1},{1,–1} were not separable and were fitted as a 1:1.2:1 weighted sum that follows from the approximate ratio of Gaussian peaks heights used to fit the band (Fig. 3*F*). A global fit (Fig. 3 *A*–*D*) of the four resultant Bragg profiles of the six peaks allowed us to estimate (7, 21, 38) the tilt t to be less than 8°and the twist α to be 47° (Fig. 3). The tilt direction ψ is 30° away from the nearest neighbor.

After fitting the Bragg rods, the complete set of Bragg intensities in Table 1 was fitted using Eq. **1** integrated over Q_z to find α, t, and ψ again in a way more sensitive to α and ψ. This resulted in two fitted minima for (α, t, ψ) at (47.9°, 2.0°, 32.9°) and (20.9°, 2.0°, 59.2°). This is due to the 2D nature of the GIXD measurement at the interface which makes a unique determination of the orientation of the rotors in the unit cell impossible. We can rule out the latter set of angles as unphysical, because they lead to overlapping triptycene groups.

X-Ray Reflectivity. X-ray specular reflectivity $R(Q_z)$, normalized to $R_F(Q_z)$, provides information about ρ(z), where z is the distance from the surface (the top of the monolayer):

$$R(Q_z) = R_F(Q_z)\left|\rho_\infty^{-1}\int \mathrm{d}\rho(z)/\mathrm{d}z\,\exp(iQ_z z)\mathrm{d}z\right|^2, \qquad [2]$$

where ρ_∞ is the electron density of bulk water (0.3334 e^-/Å^3) (39). Surface roughness σ arises from thermal surface capillary waves and is treated by smoothing the electron density gradient at the slab boundary from a delta function to a Gaussian with FWHM proportional to σ. $R(Q_z)$ was fitted in several ways (Fig. 4). The required electron density ρ($\boldsymbol{r}$) for an isolated molecule of the Cs salt of **1** on a water surface was calculated by the BP86-D3 (40, 41, 42)/def2-TZVP (43, 44) method (Fig. 5).

Model A. A very simple three-slab model (He - head - tail - subphase) and the kinematic modeling method (38) give a reasonable three-parameter fit with a uniform ρ = 0.384 e$^-$/Å^3 and length L = 29.7 ± 2.8 Å (Fig. 4). The surface roughness σ is 5.24 ± 0.10 Å. The length L agrees well with that obtained from the calculated electron density map, but the electron density disagrees with the value estimated from $n_e/(L \times \mathrm{mmA}) = 473\ e^-/(29.7$ Å × 59.8 Å^2) = 0.27 e^-/Å.

Model B. The calculated electron density map is represented by a stack of eight slabs [He + six rotor slabs + subphase (Table 2)]. The fitted curve (Fig. 4) also agrees with the data and shows a better fit to the calculated electron density. This model does, however, require an unusually large value for the surface roughness (σ = 14.0 ± 0.89 Å^{-1}, ρ = 0.334 e^-/Å^3) in the slab that includes the dipole rotator.

Model C. The calculated electron density of Fig. 1 was directly used with Eq. **1**. Surprisingly, only poor fits were obtained from this more rigorous method (Fig. 4). All attempted fits with this model produced a reflectivity decreasing immediately with Q_z instead of rising first. An investigation revealed that this was caused by the sharp drop in e^- density in the inner portion of the film above and below the dipolar rotator at the acetylene groups, and the artificial introduction of extra electron density anywhere between the decks leads to the qualitatively correct behavior of the reflectivity but not necessarily a good fit.

Model D. Electron density was augmented by placing water molecules near the rotator. The fitted curve (Fig. 4) now fits the data

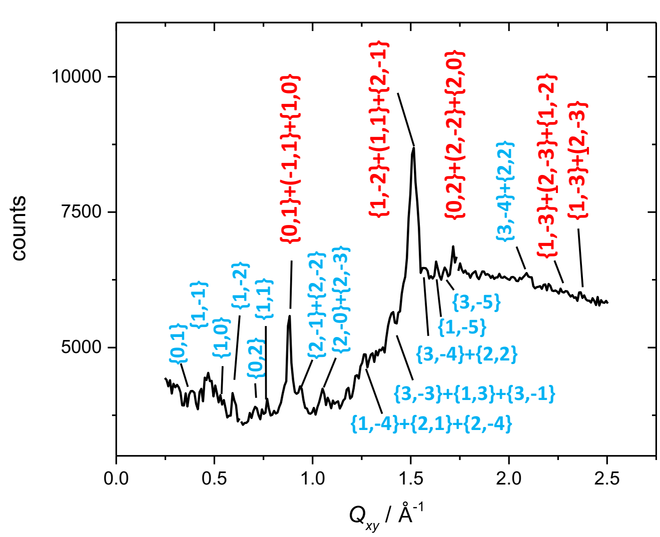

Fig. 2. GIXD of **1** on 10 mM aqueous CsCl at 30 mN/m. Red indices: major lattice. Blue indices: minor lattice. Cf. Fig. S5 for GIXD of **1** on neat H_2O at 30 mN/m, demonstrating the reproducibility of the minor lattice scattering peak positions and their variable intensity relative to the major lattice.

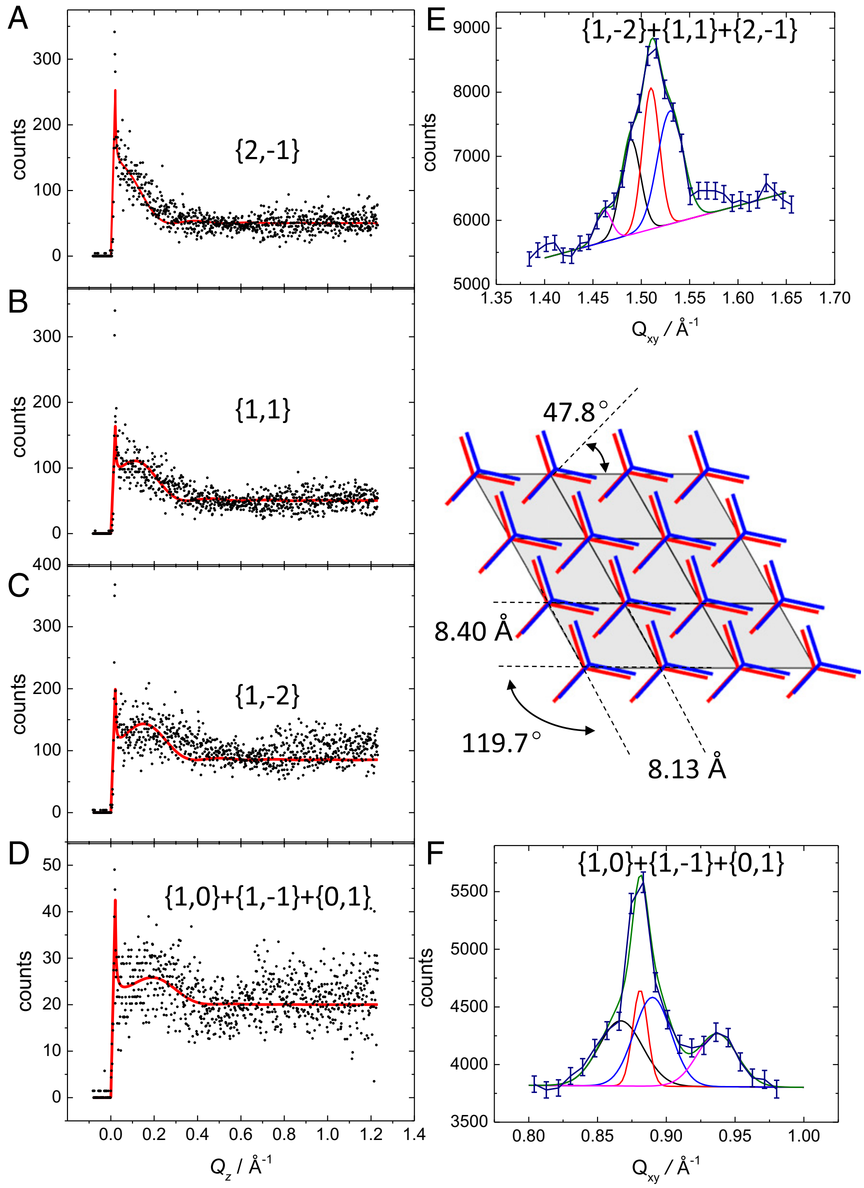

Fig. 3. (*A–D*) Simultaneous fits to the Bragg rod profiles for the six most intense peaks indexed for the major lattice. (*E* and *F*) Decomposition of the overlapping peaks. A rotor lattice schematic is shown as an inset. The displacement of the upper rod (blue) relative to the lower rod (red) due to the tilt is also shown.

well with the correct initial behavior of the reflectivity, and requires just three adjustable parameters: σ, *t*, and a scaling factor. The best fit was obtained for the addition of seven H_2O molecules (discussed below).

Molecular Modeling. An effort was made to reproduce the observed major lattice computationally. A grid of four molecules of the Cs salt of **1** on 120 molecules of water was used to model an infinite 2D lattice using cyclic boundary conditions. The size of the unit cell was 57.5 Å^2, chosen to reproduce the mmA determined from Langmuir isotherms. The lattice constants were $\alpha = \beta = 90°$, $\gamma = 120°$, $a = 16.0$ Å, $b = 16.6$ Å, and $c = 60.0$ Å. After structure optimization [PM6 (45) in the quickstep module (46) of the CP2K 4.1 (47) program package; correction for dispersion is not available], the monolayer maintained the trigonal arrangement. The average tilt angle of all four LB molecules was ∼4° and the distance between the nearest rotors was ∼8.0 Å (Fig. 5). A projection of the electron density into the surface normal was first calculated with 0, 6, 12, and 24 equilibrated molecules of water present between the two triptycene decks (Fig. S4). The equilibration spread the water quite evenly below and above the rotator; most of it was at the C–Cl dipoles (Fig. S4). Then, equilibration was done for five to eight water molecules and the best fit was found for seven. Numerous alternative arrangements of the water molecules around the rotator are possible, but all seem to yield fits of the same quality.

Minor Lattice. The remaining scattering peaks (Table 1) fit a different indexing scheme (blue in Fig. 2) with unit cell dimensions of 14.9 ± 0.1 Å × 9.13 ± 0.1 Å, with an angle of 115.0 ± 0.8°, and a total area of 122.9 Å^2 (i.e., two rotors at 61.5 Å^2 per rotor). Most peak intensities were too weak for the global Bragg rod fitting approach and the exact number and positions of the rotors in the unit cell could not be assigned with certainty. The out-of-plane scattering intensity in two Bragg rod profiles (Q_{1-1} and Q_{1-2}) suggests $t = \sim 57°$ from a simple geometric argument, $t = \tan^{-1}(Q_z/Q_{hk})$, and rules out the assignment of these peaks to a superlattice of Cs^+ cations just below the interface (16).

Discussion

Synchrotron GIXD has been often used on fatty acid monolayers but to our knowledge never for a detailed analysis of an assembly of molecules as complex as **1**. It is a pleasant surprise that the method is so useful for establishing the monolayer structure of **1**, especially in the simultaneous presence of two crystalline phases. It even allowed the detection of extraneous water molecules in the monolayer.

The results are encouraging for the potential development of 2D ferroelectrics, in that under the right conditions rotor **1** forms a monolayer with a lattice that appears perfect for ferroelectric behavior. In addition to ideal symmetry and upright orientation of rotational axes it offers significantly shorter interrotor distances and an order-of-magnitude larger domains than the surface inclusion compounds with which we have also been working. According to approximate theory (48), the dipole-to-dipole distance of 8.3 Å and a dipole of ~2.5 Debye (49) promise a Curie temperature $T_C = \sim 120$ K in the absence of defects. The use of a larger dipole would raise it further; for pyridazine (4) [μ = ~4 Debye (50)] the expectation is $T_C = \sim 300$ K.

Still, formidable obstacles remain, since it is not obvious that the structure can be transferred to a solid substrate unperturbed. Even if it can, it may collapse after evaporation of the water, whose presence in the monolayer reduces the dipole moment and possibly hinders the rotation. It may be necessary to examine the assembly of **1** directly on a solid surface (33), giving up the surface pressure degree of freedom and easy annealing offered by a Langmuir trough during monolayer preparation. It may also be necessary to modify the structure of the molecular rotor in ways that will make the monolayer sturdier (e.g., by cross-linking).

The performance of the PM6 method without dispersion correction in simulating the experimental results is reasonable and the structure of the lattice of **1** is reproduced well, including the twist of the rotor.

The large albeit inaccurately known average tilt angle in the minor lattice suggests that it probably has a structure in which the top layer is not interlocked, and this is compatible with the observation that its fraction is larger at very low surface pressures (very large mmA). It may be possible to eliminate it entirely from the film by annealing before transfer is attempted.

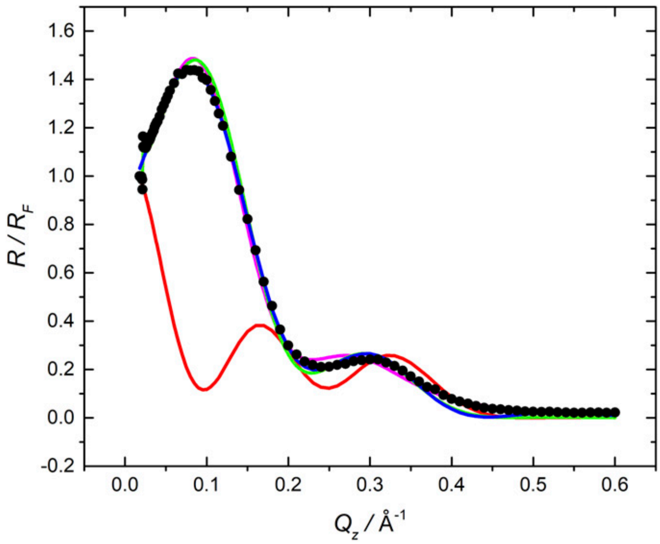

Fig. 4. Fits of X-ray reflectivity. Black circles: Normalized reflectivity curve for **1** on 10 mM CsCl at 30 mN/m. The diameter of the circles approximates the experimental error. Fits: green, four-slab model A; purple, eight-slab model B; red, calculated e^- density for **1**, model C; blue, calculated e^- density including contribution from seven H_2O molecules near the rotator, model D.

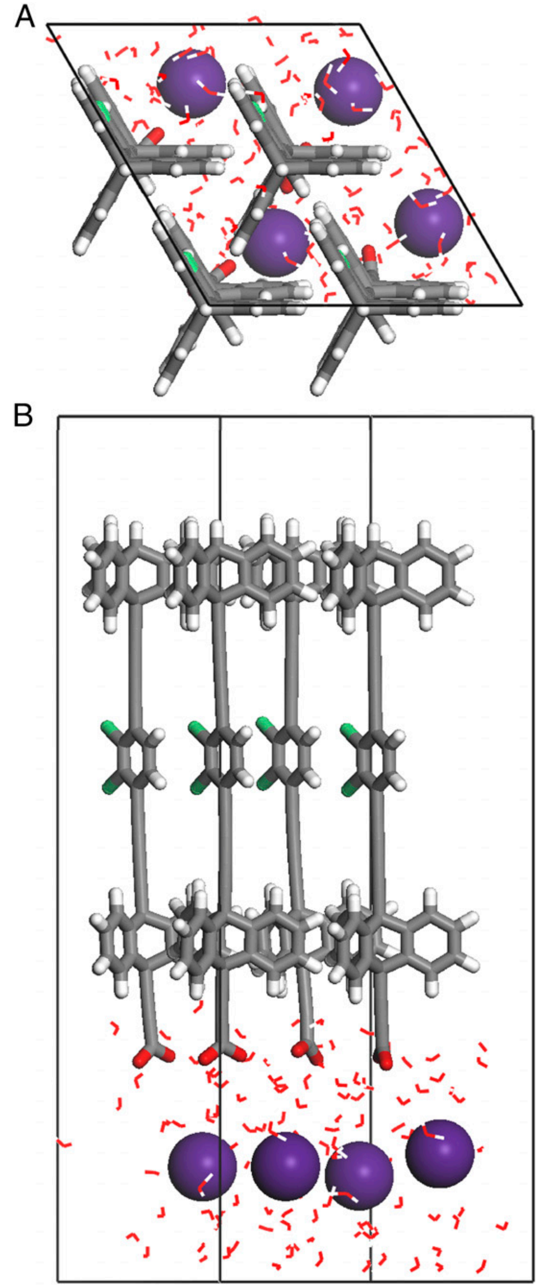

Fig. 5. Top (*A*) and side (*B*) view of PM6-optimized structure of the major phase of Cs salt of **1** on water.

Materials and Methods

GIXD and reflectivity were measured at the ChemMatCARS facility at the Advanced Photon Source at Argonne National Laboratory. The equipment and experimental methods have been previously described (51). The best GIXD results were obtained by sonicating **1** in a THF solution for a least 10 min, applying a known amount to an aqueous surface, and compressing the film to 30 mN/m at a compression rate of 1 mm/min. All measurements were done at room temperature under a He purge with O_2 levels less than 1%. The energy of the beam was 10 keV (λ = 1.23984 Å) with a resolution-limited diffraction peak FWHM of 0.0134 Å^{-1} for the slit combination along the detector beam. Fresh spreading solutions of **1** in tetrahydrofuran (~100 μM) were sometimes sonicated for 10 min before use. "Burn" tests, performed to assess the stability of the monolayers to degradation under a continuously purged He atmosphere, indicated that **1** had a ~90-min half-life in the beam. A step and collect procedure was used to minimize the cumulative damage in each beam spot: The trough was translated under the beam by a few millimeters to ensure a fresh spot at the start of each diffraction or reflectivity scan.

ACKNOWLEDGMENTS. We thank Dr. Binhua Lin, Dr. Mati Meron, and Dr. Wei Bu of the ChemMatCARS facility of the University of Chicago for helpful discussions and assistance with the measurements. Work in Prague was supported by the European Research Council (ERC) under the European Community's Framework Programme (FP7/2007-2013) ERC Grant 227756 and by the Institute of Organic Chemistry and Biochemistry, Academy of Sciences of the Czech Republic (RVO: 61388963). Work in Boulder was supported by National Science Foundation Grant DMR 1608424. ChemMatCARS Sector 15 is principally supported by the Divisions of Chemistry (CHE) and Materials Research (DMR), National Science Foundation, under Grant NSF/CHE-1346572. Use of the Advanced Photon Source, an Office of Science User Facility, operated for the US Department of Energy (DOE) Office of Science by Argonne National Laboratory, was supported by the US DOE under Contract DE-AC02-06CH11357.

1. Zhao K, Dron PI, Kaleta J, Rogers CT, Michl J (2014) Arrays of dipolar molecular rotors in tris(o-phenylenedioxy)cyclotriphosphazene (TPP) topics in current chemistry. *Molecular Machines and Motors: Recent Advances and Perspectives*, eds Credi A, Silvi S, Venturi M (Springer, Cham, Switzerland), pp 163–211.
2. Rozenbaum VM (1996) Coulomb interactions in two-dimensional lattice structures. *Phys Rev B* 53:6240–6255.
3. Catalano L, et al. (2017) Rotational dynamics of diazabicyclo[2.2.2]octane in isomorphous halogen-bonded co-crystals: Entropic and enthalpic effects. *J Am Chem Soc* 139:843–848.
4. Dron PI, et al. (2016) Bulk inclusions of pyridazine-based molecular rotors in tris(o-phenylene)cyclotriphosphazene (TPP). *Adv Funct Mater* 26:5718–5732.
5. Roberts GG (1990) *Langmuir Blodgett Films* (Plenum, New York).
6. Kaleta J, Kaletová E, Císařová I, Teat SJ, Michl J (2015) Synthesis of triptycene-based molecular rotors for Langmuir-Blodgett monolayers. *J Org Chem* 80:10134–10150.
7. Kjaer K, Als-Nielsen J, Helm CA, Tippman-Krayer P, Möhwald H (1989) Synchrotron X-ray diffraction and reflection studies of arachidic acid monolayers at the air-water interface. *J Phys Chem* 93:3200–3206.
8. Leveiller F, et al. (1991) Crystallinity of the double layer of cadmium arachidate films at the water surface. *Science* 252:1532–1536.
9. Tippmann-Krayer P, Möhwald H (1991) Precise determination of tilt angles by x-ray diffraction and reflection with arachidic acid monolayers. *Langmuir* 7:2303–2306.
10. Tippmann-Krayer P, Kenn RM, Möhwald H (1992) Thickness and temperature dependent structure of Cd arachidate Langmuir-Blodgett films. *Thin Solid Films* 210–211:577–582.
11. Leveiller F, Jacquemain D, Leiserowitz L, Kjaer K, Als-Nielsen J (1992) Toward a determination at near atomic resolution of two-dimensional crystal structures of amphiphilic molecules on the water surface: A study based on grazing incidence synchrotron x-ray diffraction and lattice energy calculations. *J Phys Chem* 96:10380–10389.
12. Goldmand M, et al. (1994) In-plane X-ray diffraction from monolayers of perfluorinated fatty acids: Evidence for azimuthal ordering in the condensed phase. *J Phys II* 4:773–785.
13. Böhm C, et al. (1994) Packing characteristics of crystalline monolayers of fatty acid salts, at the air-solution interface, studied by grazing incidence X-ray diffraction. *Langmuir* 10:830–836.
14. Als-Nielsen J, et al. (1994) Principles and applications of grazing incidence x-ray and neutron scattering from ordered molecular monolayers at the air-water interface. *Phys Rep* 246:251–313.
15. Leveiller F, et al. (1994) Two-dimensional crystal structure of cadmium arachidate studied by synchrotron X-ray diffraction and reflectivity. *Langmuir* 10:819–829.
16. Kmetko J, et al. (2001) Ordering in the subphase of a Langmuir monolayer: X-ray diffraction and anomalous scattering studies. *Langmuir* 17:4697–4700.
17. Dupres V, et al. (2003) Superlattice formation in fatty acid monolayers on a divalent ion subphase: Role of chain length, temperature, and subphase concentration. *Langmuir* 19:10808–10815.
18. Pignat J, Daillant J, Leiserowitz L, Perrot F (2006) Grazing incidence x-ray diffraction on Langmuir films: Toward atomic resolution. *J Phys Chem* 110:22178–22184.
19. Vakim D, Bu W, Satija SK, Travesset A (2007) Ordering by collapse: Formation of bilayer and trilayer crystals by folding Langmuir monolayers. *Langmuir* 23:1888–1897.
20. Shih MC, Peng JB, Huang KG, Dutta P (1993) Structures of fatty acid monolayers transferred to glass substrates from various Langmuir monolayer phases. *Langmuir* 9:776–778.
21. Kjaer K (1994) Some simple ideas on X-ray reflection and grazing-incidence diffraction from thin surfactant films. *Physica B Condens Matter* 198:100–109.
22. Hazra S, Gibaud A, Désert A, Gacem V, Cowlam N (2000) X-ray scattering studies of imperfect manganese stearate Langmuir–Blodgett films. *Physica B Condens Matter* 283:45–48.
23. Kumara NP, et al. (2002) Molecular packing in cadmium and zinc arachidate LB multilayers. *Colloids Surf A* 198-200:75–78.
24. Norvez S, Simon J (1990) Epitaxygens: Mesophases based on the triptycene molecular subunit. *J Chem Soc Chem Commun* 26:1398–1399.
25. Norvez S (1993) Liquid crystalline triptycene derivatives. *J Org Chem* 58:2414–2418.
26. Yamamura K, Kawashima T, Eda K, Tajima F, Hashimoto M (2005) Solid solution of triptycenequinone and triptycenehydroquinone as a non-stoichiometric quinhydrone. Bathochromic changes in color caused by local intermolecular interaction between *p*-benzoquinone and hydroquinone moieties. *J Mol Struct* 737:1–6.
27. Chong J, MacLachlan M (2007) Synthesis and structural investigation of new triptycene-based ligands: En route to shape-persistent dendrimers and macrocycles with large free volume. *J Org Chem* 72:8683–8690.
28. Kissel P, Murray DJ, Wulftange WJ, Catalano VJ, King BT (2014) A nanoporous two-dimensional polymer by single-crystal-to-single-crystal photopolymerization. *Nat Chem* 6:774–778.
29. Kory MJ, et al. (2014) Gram-scale synthesis of two-dimensional polymer crystals and their structure analysis by X-ray diffraction. *Nat Chem* 6:779–784.
30. Seiki N, et al. (2015) Rational synthesis of organic thin films with exceptional long-range structural integrity. *Science* 348:1122–1126.
31. Payamyar P, et al. (2015) Approaching two dimensional copolymers: Photoirradiation of anthracene and diaza anthracene bearing monomers in Langmuir monolayers. *Macromol Rapid Commun* 36:151–158.
32. Murray DJ, et al. (2015) Large area synthesis of a nanoporous two-dimensional polymer at the air/water interface. *J Am Chem Soc* 137:3450–3453.
33. Leung FK-C, et al. (2016) Supramolecular scaffold for tailoring the two-dimensional assembly of functional molecular units into organic thin films. *J Am Chem Soc* 138:11727–11733.
34. Payamyar P, King BT, Öttinger HC, Schlüter DA (2016) Two-dimensional polymers: Concepts and perspectives. *Chem Commun (Camb)* 52:18–34.
35. Pershan PS, Schlossman ML (2012) *Liquid Surfaces and Interfaces: Synchrotron X-Ray Methods* (Cambridge Univ Press, Cambridge, UK).
36. Vaknin D, Bu W, Traversset A (2008) Extracting the pair distribution function of liquids and liquid-vapor surfaces by grazing incidence x-ray diffraction mode. *J Chem Phys* 129:044504.
37. Vineyard GH (1982) Grazing-incidence diffraction and the distorted-wave approximation for the study of surfaces. *Phys Rev B* 26:4146–4159.
38. Als-Nielsen J, Kjaer K (1989) X-ray reflectivity and diffraction studies of liquid surfaces and surfactant monolayers. *Phase Transitions in Soft Condensed Matter*, eds Riste T, Sherrington D (Springer, New York), pp 113–138.
39. Tomberli B, Benmore CJ, Egelstaff PA, Neuefeind J, Honkimäki V (2000) Isotopic quantum effects in water structure measured with high energy photon diffraction. *J Phys Condens Matter* 12:2597–2612.
40. Becke AD (1988) Density-functional exchange-energy approximation with correct asymptotic behavior. *Phys Rev A* 38:3098–3100.
41. Perdew JP (1986) Density-functional approximation for the correlation energy of the inhomogeneous electron gas. *Phys Rev B* 33:8822–8824.
42. Grimme S, Antony J, Ehrlich S, Krieg H (2010) A consistent and accurate ab initio parametrization of density functional dispersion correction (DFT-D) for the 94 elements H-Pu. *J Chem Phys* 132:154104.
43. Weigend F, Ahlrichs R (2005) Balanced basis sets of split valence, triple zeta valence and quadruple zeta valence quality for H to Rn: Design and assessment of accuracy. *Phys Chem Chem Phys* 7:3297–3305.
44. Weigend F (2006) Accurate coulomb-fitting basis sets for H to Rn. *Phys Chem Chem Phys* 8:1057–1065.
45. Stewart JJP (2007) Optimization of parameters for semiempirical methods V: Modification of NDDO approximations and application to 70 elements. *J Mol Model* 13:1173–1213.
46. Vande Vondele J, et al. (2005) Quickstep: Fast and accurate density functional calculations using a mixed Gaussian and plane waves approach. *Comput Phys Commun* 167:103–128.
47. The CP2K developers group. (2016) CP2K: Open source molecular dynamics. Available at https://www.cp2k.org/. Accessed April 4, 2016.
48. Rozenbaum VM, Ogenko VM, Chuiko AA (1991) Vibrational and orientational states of surface atomic groups. *Sov Phys Usp* 34:883–902.
49. Hurdis EC, Smyth CP (1942) Dipole moments in the vapor state and resonance effects in some substituted benzenes. *J Am Chem Soc* 64:2212–2216.
50. Li H, Franks KJ, Hanson RJ, King W (1998) Brute force orientation and alignment of pyridazine probed by resonantly enhanced multiphoton ionization. *J Phys Chem A* 102:8084–8090.
51. Lin B, et al. (2003) The liquid surface/interface spectrometer at ChemMatCARS synctrotron facility at the advanced photon source. *Physica B* 336:75–80.